JGR Solid Earth

Key Points:

- We develop a framework for systematically locating fault zones at sub-kilometer scales using the distributed acoustic sensing-measured earthquake wavefield
- We present a model for these fault zones and use simulations to show that this model reproduces first-order observations of scattering
- By comparing observations with synthetics, we use this method to constrain local fault zone geometry

Correspondence to:

J. Atterholt,
atterholt@caltech.edu

Author Contributions:

Conceptualization: James Atterholt, Zhongwen Zhan
Data curation: James Atterholt
Formal analysis: James Atterholt, Zhongwen Zhan
Funding acquisition: James Atterholt, Zhongwen Zhan
Investigation: James Atterholt, Zhongwen Zhan, Yan Yang
Methodology: James Atterholt, Zhongwen Zhan, Yan Yang
Project Administration: Zhongwen Zhan
Resources: Zhongwen Zhan
Software: James Atterholt
Supervision: Zhongwen Zhan
Validation: James Atterholt, Yan Yang
Visualization: James Atterholt
Writing – original draft: James Atterholt

Fault Zone Imaging With Distributed Acoustic Sensing: Body-To-Surface Wave Scattering

James Atterholt[1] , **Zhongwen Zhan[1]** , **and Yan Yang[1]**

[1]Seismological Laboratory, California Institute of Technology, Pasadena, CA, USA

Abstract Fault zone structures at many scales largely dictate earthquake ruptures and are controlled by the geologic setting and slip history. Characterizations of these structures at diverse scales inform better understandings of earthquake hazards and earthquake phenomenology. However, characterizing fault zones at sub-kilometer scales has historically been challenging, and these challenges are exacerbated in urban areas, where locating and characterizing faults is critical for hazard assessment. We present a new procedure for characterizing fault zones at sub-kilometer scales using distributed acoustic sensing (DAS). This technique involves the backprojection of the DAS-measured scattered wavefield generated by natural earthquakes. This framework provides a measure of the strength of scattering along a DAS array and thus constrains the positions and properties of local scatterers. The high spatial sampling of DAS arrays makes possible the resolution of these scatterers at the scale of tens of meters over distances of kilometers. We test this methodology using a DAS array in Ridgecrest, CA which recorded much of the 2019 M_w7.1 Ridgecrest earthquake aftershock sequence. We show that peaks in scattering along the DAS array are spatially correlated with mapped faults in the region and that the strength of scattering is frequency-dependent. We present a model of these scatterers as shallow, low-velocity zones that is consistent with how we may expect faults to perturb the local velocity structure. We show that the fault zone geometry can be constrained by comparing our observations with synthetic tests.

Plain Language Summary Fault zones are multi-scale structures that govern where and how earthquakes happen. Characterizing fault zones at all scales is thus important for understanding earthquake ruptures and earthquake-related hazards. However, finding and describing fault zones at small scales remains a persistent challenge in earthquake science. We propose a framework for the characterization of fault zones using distributed acoustic sensing (DAS), a recently developed technique that converts fiber optic cables into dense networks of ground motion sensors. Earthquake waves are scattered when they encounter fault zones, and this scattering creates signatures in DAS data that we can use to locate these fault zones. Additionally, the behavior of fault zone scattered waves with frequency may illuminate detailed characteristics of the fault zone. We test this framework using a DAS network in Ridgecrest, CA that recorded aftershocks of the 2019 magnitude 7.1 Ridgecrest earthquake. We use these recordings to map fault zone locations near the network. These locations are close to previously mapped faults but are more accurate. By comparing the behavior of observed fault zone scattered waves with frequency with that of simulations, we can constrain shallow fault zone geometry.

1. Introduction

The Earth's crust is a geologically heterogeneous medium that hosts myriad sharp material contrasts at multiple scales. Among these heterogeneities are fault zones, features consisting of fault cores and surrounding zones of fracture that accommodate strain. Finding new ways to locate and characterize fault zones may potentially serve a variety of societally and scientifically important functions. Proximity to fault zones increases the likelihood of severe damage to infrastructure, both because fault zones host static deformation, and because fault zones may amplify ground motion (Kurzon et al., 2014). Additionally, the locations of faults control estimates of fault connectivity, which is an important parameter in some probabilistic hazard estimates (Field et al., 2014). Relatedly, relative fault positioning and fault geometry play a pivotal role in the propagation and termination of earthquakes (Harris & Day, 1993, 1999; Wesnousky, 2008). Fault damage zone scaling is expected to play an influential role in earthquake nucleation (Ampuero et al., 2002), earthquake potency (Weng et al., 2016), and long-term earthquake sequence behavior (Thakur et al., 2020). Importantly, fault zones are multi-scale structures (Faulkner et al., 2010), and thus developing a more complete picture of fault zone structure at sub-kilometer scales contributes to these efforts to evaluate earthquake hazard and geological controls on earthquake phenomenology.

**Writing – review & editing:** James Atterholt, Zhongwen Zhan, Yan Yang

Considerable attention is given to major fault zones, those that are large and accommodate significant strain. But, minor and unmapped fault zones are an important consideration when evaluating the structural deformation and earthquake hazards in a region. Plate deformation is usually not accommodated by a single fault zone, but rather by a broad distribution of fault zones that extend sometimes hundreds of kilometers from the plate boundary, and minor fault zones play a key role in the accommodation of this strain (Scholtz, 2019). In the absence of high deformation rates, minor fault zones can develop a high risk potential if strain accumulates over a long time period, the stress state changes (Freed & Lin, 2001), or the stability of the fault is perturbed (Ellsworth, 2013). Relatedly, many significant earthquakes rupture within minor or unmapped fault zones. For example, the 2019 Ridgecrest earthquake sequence, which included the largest earthquake to take place in California in over two decades, ruptured mostly unmapped faults in the Little Lake and Airport Lake fault zones (Ross et al., 2019), which only accommodated approximately 1 mm/y of slip (Amos et al., 2013).

For both major and minor fault zones, shallow fault zone structure is important. The shallowest few hundred meters of fault zones can exhibit sharp and localized velocity reductions (e.g., Share et al., 2020; Wang et al., 2019; Zigone et al., 2019) that can amplify ground motion, and shallow crustal faults play an important role in both facilitating and impeding the transport of groundwater and hydrocarbons (Bense et al., 2013). Shallow fault zone structure may also be used to infer the contribution of deep fault structure, which is very difficult to constrain, by correcting for shallow structure contributions in depth-integrated fault characterization approaches.

Previous efforts to locate and describe shallow fault zone structures at sub-kilometer scales have typically relied on geologic mapping, seismic surveying, and satellite imagery. Geologic mapping over decades has produced excellent records of Quaternary faults (e.g., USGS and CGS, 2022), but discerning faults using geologic mapping requires careful fieldwork and evidence of faulting at the surface. Seismic surveying produces detailed images of the subsurface, with which fault locations can be inferred (e.g., Lay et al., 2021; Liberty et al., 2021), but surveys are often expensive and logistically challenging, particularly in urban settings. Satellite imagery is also used to map faults, often by identifying topographic anomalies in images (Joyce et al., 2009). More involved processing, such as producing phase gradient maps from InSAR interferograms (Xu et al., 2020), can also be used to identify fractures. These techniques are powerful, but they require surficial evidence of strain that can be imaged from above.

Other studies have used the earthquake wavefield to characterize the structure of major fault zones. For example, some studies have used fault zone head waves, head waves generated by refraction due to a bimaterial contrast across the fault, to image the fault interface and constrain the velocity contrast across the fault (e.g., Allam et al., 2014; McGuire & Ben-Zion, 2005; Qin et al., 2020; Share & Ben-Zion, 2018). Additionally, some studies have used travel-time anomalies from regional and teleseismic events to discern properties like the width of the damage zone and the velocity reduction within the damage zone (e.g., Cochran et al., 2009; Qiu et al., 2021; Share et al., 2022; Yang et al., 2020). Moreover, low velocity structures can amplify ground motion, and some studies have used S-wave amplification caused by the reduced velocities in fault damage zones to delineate their structure (e.g., Qiu et al., 2021; Song & Yang, 2022). Another approach is to use fault zone trapped waves, waves generated by constructive interference of critically reflected waves in the fault damage zone, which can be initiated by sources outside the fault zone (Fohrmann et al., 2004) and have been used to constrain the structure of fault damage zones (e.g., Ben-Zion et al., 2003; Catchings et al., 2016; Qiu et al., 2021; Wang et al., 2019). In general, these techniques are highly effective tools for capturing geometric and internal properties of major fault zones. But, fault zones usually need to exhibit relatively large and spatially consistent elastic material contrasts for these techniques to be used. Hence, these techniques are typically applied to major fault zones using targeted deployments of dense networks of sensors. These factors make these methods ineffectual for the discovery and characterization of minor fault zones.

The weaknesses of these methods motivate the development of complimentary techniques for identifying and characterizing sub-kilometer scale fractures in the crust. To this end, we suggest an alternative method for identifying and characterizing fractures in the crust using distributed acoustic sensing (DAS) data. DAS is an emergent technology that repurposes fiber optic cables as dense arrays of strainmeters. DAS uses a laser interrogator unit to emit pulses of light that probe a fiber optic cable, and natural imperfections in the fiber send echoes back to the interrogator unit. Perturbations of the fiber change the travel times of these echoes, and these changes in travel time are quasi-linearly proportional to the strain induced by the perturbations. The high spatial frequency of DAS data allows for the resolution of high wavenumber phenomena that are incoherent in more sparsely measured
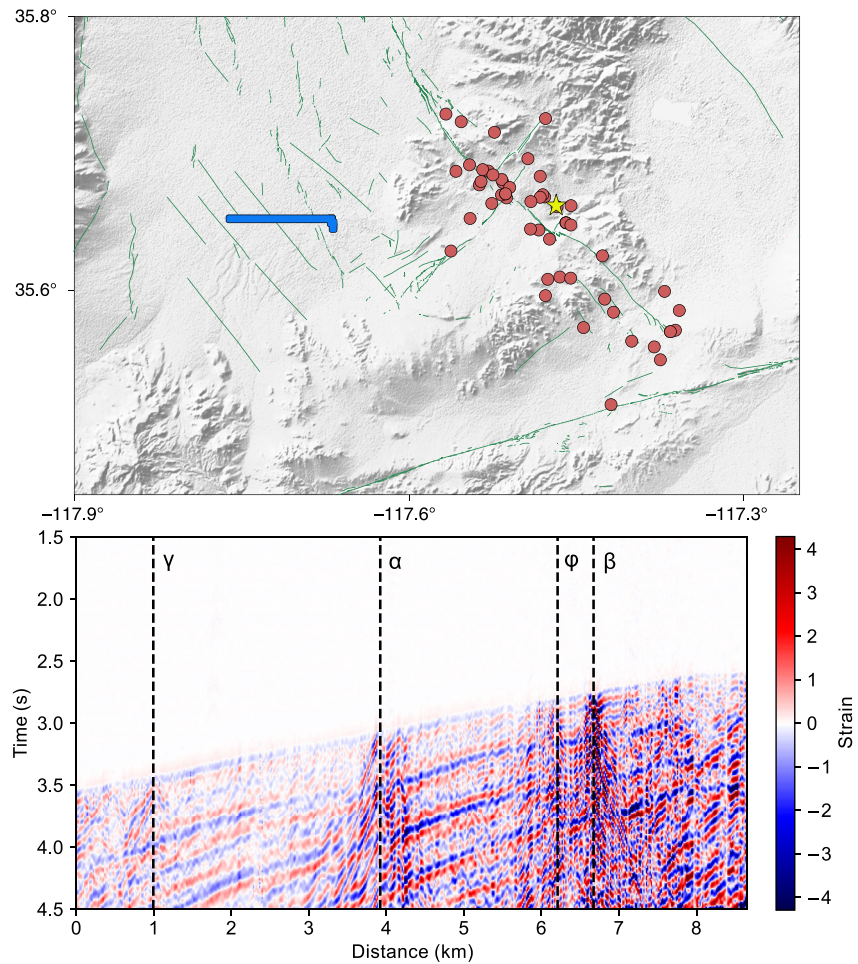
Figure 1. (Top) The geographic setting of the data used in this study. Blue line corresponds to the distributed acoustic sensing (DAS) array. Red dots correspond to the epicenters of the events used in this study. Yellow star corresponds to the epicenter of the event shown below (depth 5.6 km). Green lines correspond to the USGS-mapped Quaternary faults in the area. (Bottom) Example of the DAS-measured wavefield of the onset of an event used in this study. Black dotted lines correspond to the locations of the chevron-like features that are mapped in Figure 3.

data, which is useful for characterizing fault zones at high resolution (Jousset, 2019). One such phenomenon is the scattering of earthquake body waves to surface waves due to small-scale, local heterogeneities in the upper crust. We show an example of this scattering in Figure 1, and we subsequently refer to these features as chevrons, owing to their chevron-like shape in DAS data representations. These chevrons have been observed in other DAS datasets, and the scatterers generating these chevrons have been inferred to be faults (Lindsey et al., 2019; Spica et al., 2020). Moreover, these scattered surface waves are also visible in empirical Green's functions derived in DAS datasets that can be migrated to infer scatterer locations (Cheng et al., 2021; Yang, Zhan, et al., 2022).

Our contributions in this paper are as follows. We suggest a local backprojection framework for the systematic location of the sources of these chevron-like features and find a strong spatial correlation between these locations and mapped faults. We suggest a model of these scatterers as rectangular perturbations in the velocity field, approximating a fault zone, and show that this model reproduces first-order features observed in the data. We then show that we can constrain key geometric features of the fault zone under this backprojection framework.
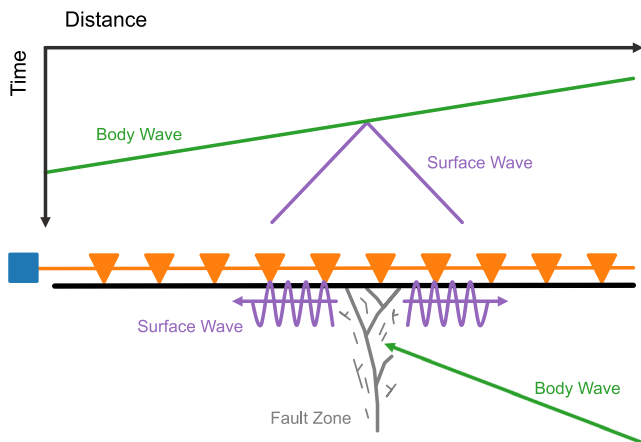
Figure 2. Schematic illustration of the phenomena observed in the earthquake wavefields used in this study. (Top) Record section corresponding to the processes illustrated below. (Bottom) Illustration of the phenomena resulting in the generation of the chevron-like features shown in Figure 1. Colors represent the same phenomena in both top and bottom. Green corresponds to incident body wave. Gray features indicate a fault zone. Purple corresponds to the scattered surface waves resulting from the body waves impinging on the fault zone. Orange line and triangles indicate the fiber optic cable and stations, respectively. Blue box represents the distributed acoustic sensing interrogator unit.

2. Data

In early July 2019, a large earthquake sequence initiated in the Eastern California Shear Zone. This sequence, which included a M_w6.4 foreshock and a M_w7.1 mainshock, produced thousands of aftershocks over the course of a few months. Shortly following the mainshock, a DAS array was deployed in Ridgecrest, CA using an Optasense ODH3 interrogator unit in an effort to record this aftershock sequence (Li et al., 2021). This DAS array began recording on 10 July 2019, and in this study we use recorded aftershocks that took place between the initiation of recording and 4 October 2019. The array is temporally sampled at 250 Hz and is spatially sampled at 8 m intervals over 1,250 channels, with a total cable length of 10 km. The deployment of this DAS array ensured that numerous Ridgecrest sequence aftershocks were recorded nearby at a high spatial frequency.

For this study, we choose a subset of well-recorded, low-noise earthquakes on which we perform our subsequent analysis. We choose these earthquakes using straightforward quality control metrics to ensure that the earthquake wavefield has a high enough amplitude to be reliably analyzed and that the scattered surface waves are isolated from any cultural noise that may bias the analysis. As part of this quality control, we select from only events with $M_l \geq 2$ or $M_w \geq 2$ as determined by the Southern California Seismic Network catalog. We also restricted our selection to only events that occurred between 11 p.m. and 4 a.m. local time, thus only keeping events with a low probability of being partially masked by cultural noise. We then manually inspected all of the remaining events and ensured that we only kept events with negligible cultural noise. After performing this processing, we are left with 50 events that meet our quality control criteria. These events are plotted in geographic context in Figure 1. These events are reasonably well clustered by distance and azimuth, minimizing variability due to the directional sensitivity of DAS.

3. Mapping Faults Using Local Backprojection

To quantify the magnitudes and locations of these scatterers, we employ a simple local backprojection technique to identify the locus points of the scattered waves in the body wave coda. This backprojection is based on the reasonable assumption that these chevron-like waves are surface waves generated by earthquake body waves impinging on a scatterer near the DAS array. We expect this phenomenon to be body-to-surface wave scattering because the scattered waves are dispersive, which we verify subsequently, and the onset of these waves occurs early in the body wave coda. We expect these scatterers to be local because the scattered waves attenuate rapidly in space, as exemplified by the narrow width of these chevrons shown in Figure 1. Additionally, we exclude the possibility of fault resonance waves due to the fact that our resolution is approximately normal to the fault and that the chevron width, though narrow, is wider than expected for fault resonance waves for minor faults. A schematic example of the generation of these scattered waves is shown in Figure 2. The driving principle of this methodology is the same for standard backprojection techniques used in seismology (Kiser & Ishii, 2017). In particular, for grid points near or above a scatterer, the backscattered energy resultant from the scatterer will align and sum coherently, producing a larger amplitude than that of a grid point far from any scatterers. In this case, we attempt to backproject locally scattered surface waves to image the scattering source, illustrated as a fault zone in Figure 2.

To accomplish this backprojection, we first bandpass our data to a narrow frequency band; this frequency band can vary depending on the desired dimensional sensitivity. We select frequency bands with 1 Hz widths and center frequencies spanning 2–10 Hz at 0.5 Hz intervals. For each of these frequency bands, we partition the earthquake wavefield by velocity in the curvelet domain (Atterholt et al., 2021), using a curvelet basis to mute sections of the frequency-wavenumber domain and thus isolate desired wavefield components. This is equivalent to frequency-wavenumber filtering with specialized tapers that minimize velocity filtering artifacts. We use this wavefield-partitioning technique to separate the scattered wavefield and the direct waves into two separate

windows. We classify velocities below 750 m/s to be the scattered wavefield and velocities above 1,000 m/s to be the direct wavefield. We show examples of this wavefield partitioning in Figure S1 in Supporting Information S1. Of the scattered wavefield, we select only the scattered waves from the early-onset body waves, because these early-onset scattered waves are typically more pronounced relative to the earthquake wavefield and are not superimposed by earthquake-generated surface waves, which can bias the final result. To isolate the early-onset scattered waves, we window the scattered wavefield over the time interval between 2 s prior to the onset of the *P*-wave and 5 s after the onset of the *P*-wave. Once we have isolated the scattered waves, we perform a local backprojection of surface wave energy according to a local velocity model across the array. For the local velocity model, we use a 1-dimensional velocity model made by taking averages of each period of the velocity model developed by Yang, Atterholt, et al. (2022). We perform this averaging to avoid biasing of the result due to lateral slopes in the model. We then define a grid of potential scattering sources along the array geometry, and we backproject the surface waves recorded by the surrounding channels, up to a fixed distance, according to their distance from the potential source. Our grid of potential source locations is spaced at 8 m along the array, which coincides with the station spacing. In this study, by inspecting the data, we fix the maximum distance to be 250 m based on the expected distance from the chevron center over which we can expect to get significant constructive interference by aligning the waveforms. We then stack the backprojected channels and sum the absolute value of the stack, giving us an amplitude for the grid point. We only define the grid at the surface along the array, because linear DAS array geometry poorly constrains backprojection images along orthogonal axes. But, the rapid attenuation of these surface waves suggests that most of the energy in the scattered wavefield is generated very close to the array, minimizing the consequences of this poor constraint. Furthermore, scattered waves from more distant scatterers will have higher apparent velocities, minimizing the impact of these scatterers in a backprojection framework that uses true velocity.

We can verify that these scattered waves are dispersive under this framework. That is, we apply this backprojection framework to the earthquake wavefield shown in Figure 1 over a range of velocities for each frequency, rather than using a single velocity model. We can then sum across each resultant profile to get a single value for each frequency and velocity pair. From this we can determine which velocities produce the largest sum at each frequency, which we expect to be correlated with the amount of constructive interference due to waveform alignment. In this way we can construct a dispersion curve using only the scattered wavefield. This is a similar approach to that taken by Spica et al. (2022), but because we sum across the entire profile, this produces a velocity spectrum that averages the contributions of the scattered waves produced across the array. A plot of this velocity spectrum is shown in Figure S2 in Supporting Information S1. This spectrum shows a clear dispersion pattern that is well matched by the dispersive relationship for this setting computed in Yang, Atterholt, et al. (2022).

Since DAS measures longitudinal strain, which is distinct from conventional inertial seismometers, the sensitivity of DAS to these scattered waves is also distinct. For surface waves generated by scattering from a fault that runs orthogonal to the array, the recorded surface waves will propagate parallel to the fiber. Consequently, a significant component of the particle motion will be parallel to the fiber, motion to which DAS is most sensitive. For a fault that runs oblique to the array, the surface waves will not propagate exactly parallel to the fiber, and the apparent velocity will increase and the sensitivity of the DAS array to the waves will decrease. However, since these waves attenuate rapidly in space, the majority of the recorded energy will have been scattered very close to the array, minimizing variability due to obliquity. Additionally, because DAS is more sensitive to lower velocities, surface waves are amplified in DAS data relative to the other components of the earthquake wavefield. This potentially explains why these surface waves are such a common and well-recorded observation in DAS data (e.g., Ajo-Franklin et al., 2022; Lindsey et al., 2019; Spica et al., 2020). These factors suggest that the variability in scattered waves measured across the DAS array is largely due to variability in the strength and geometry of the scatterers near the array. Additionally, because we're using array seismology, we need to consider apparent velocity when performing velocity filtering and backprojecting these waves. But, since the recorded surface waves propagate approximately parallel to the fiber, the apparent velocity of locally scattered surfaces waves is very close to the true velocity. In particular, the apparent velocity follows $v_t/\cos(\theta)$; where v_t is the true velocity and θ is the incident angle relative to the array geometry. In the case of surface waves scattered very close to the array, θ is close to zero.

We apply this backprojection technique to the 50 high quality events recorded by the DAS array in Ridgecrest, CA described in the preceding section. Backprojecting the scattered wavefields of these earthquakes results in an ensemble of profiles of scattering across the Ridgecrest DAS array. To ensure that the within-array and
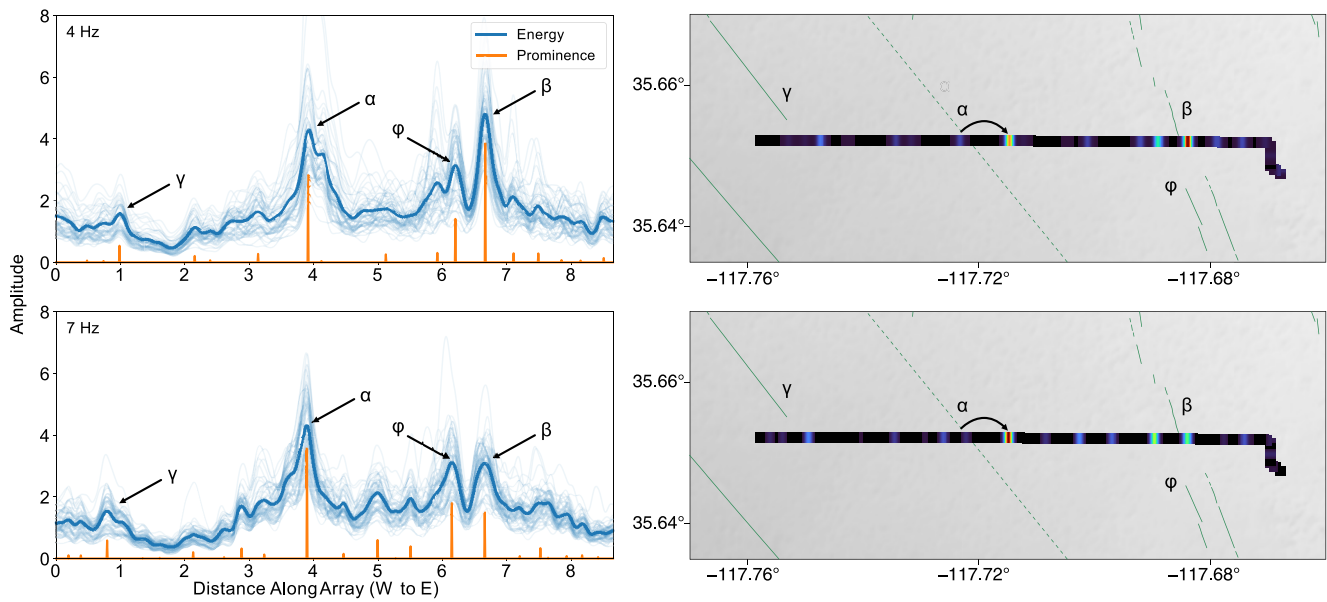
Figure 3. (Left) Backprojection profiles made using 50 events recorded by the distributed acoustic sensing (DAS) array in Ridgecrest, CA. Light blue lines correspond to profiles made using a single event. Dark blue lines correspond to the mean profile. Orange lines correspond to the topographic prominence of the mean energy profile. Top and bottom plots correspond to profiles generated with 4 and 7 Hz center frequencies, respectively. Black arrows point to referenced peaks α, β, γ, and ϕ. (Right) Prominence profiles to the left, convolved with a Gaussian kernel to widen peaks for representation, plotted on the DAS array geometry shown in Figure 1. Color corresponds to prominence amplitude. Green lines correspond to fault locations. Solid lines are moderately or well constrained fault locations, and dotted lines are inferred fault locations. Faults are labeled according to associated peaks indicated in the profiles to the left. Curved black arrows indicate the proposed relocation of the fault associated with peak α.

between-event amplitudes are comparable, we normalize the profile amplitudes by the sum of the absolute value of the body waves that occupy the same window used for each grid point in each profile. For this normalization, we account for the variability in azimuth and incident angle according to the directional sensitivity of strainmeters (Benioff, 1935). In particular, noting that the dominant body wave signal we use for this normalization is the *P*-wave, we divide the direct wavefield by $\cos^2(\theta)$. Although this normalization is imperfect, because some windows may include *P*-to-*S* conversions or *S*-waves; we find it to be sufficient for our purposes. We smooth these profiles with a Gaussian kernel with a standard deviation of five channels to minimize any high-frequency, stochastic variability in these profiles. We show these ensembles of backprojection profiles computed at 4 and 7 Hz center frequencies in Figure 3. These profiles are generally "bumpy," and it can be difficult to determine to which of these peaks to assign significance. Additionally, some peaks are of low amplitude, but are noteworthy because they are positioned in areas with low noise floors. To help us determine which peaks are most likely associated with scatterers, we use the metric from mountaineering of topographic prominence, which is a measure of the height of a peak relative to its surroundings. We plot the prominence profiles alongside the backprojection amplitude profiles in Figure 3. Additionally, we superimpose these prominence profiles on the DAS array geometry in Figure 3. Indeed, there is a spatial correlation between peaks in the prominence profile and the locations of USGS-mapped Quaternary faults near the array. This spatial correlation partially evidences the argument that the nearly ubiquitous chevron-like features in the DAS measured wavefield are fault-zone scattered waves. In Figure 3, we make note of four peaks, which we term peaks α, β, γ, and ϕ. These are the most prominent peaks in both frequency bands, and by visual inspection we can associate these peaks with mapped faults nearby. In particular, peaks α and β are noteworthy in that they are prominent enough that we can analyze their behavior with space and frequency. We use peaks α and β to infer properties of the associated fault zones subsequently.

4. Modeling Scatterers as Fault Zones

To further investigate the nature of the sources of scattering evident in DAS data, we present a model for these scatterers as rectangular perturbations in the 2D velocity structure. Although natural faults are neither perfect rectangles nor uniform velocity perturbations, this simple parameterization allows us to capture first order structural properties of fault zones without including more complexity than we can feasibly resolve given our data. The
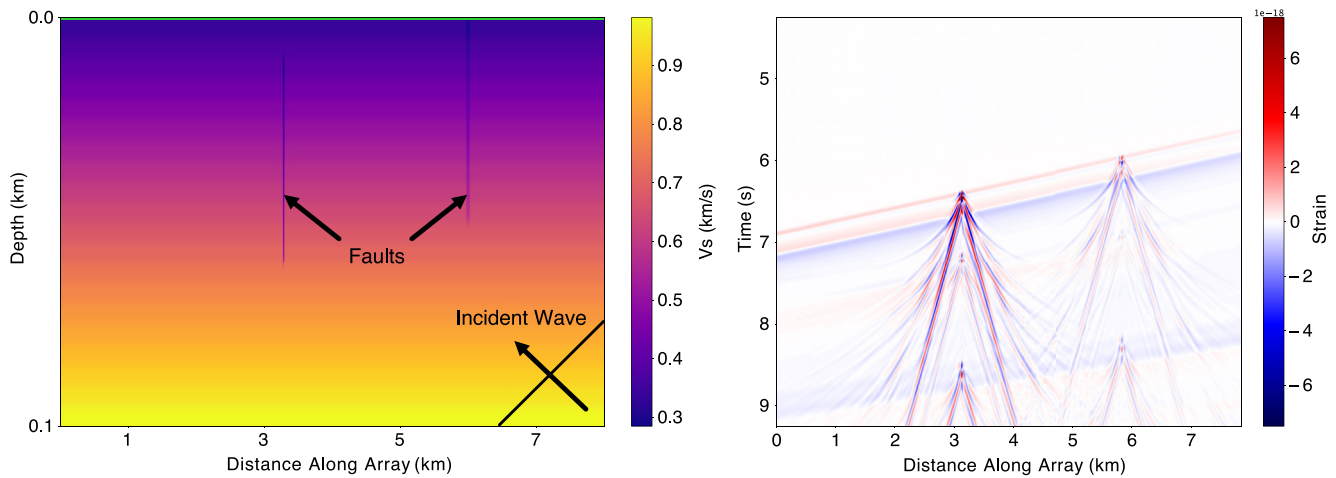
Figure 4. (Left) Example of velocity model modified from (Yang, Atterholt, et al., 2022) and (Small et al., 2017) with two fault zone-approximating velocity perturbations emplaced in the model. Green line corresponds to array of strainmeters. Black arrows point to incident wave direction and fault locations. Note the large vertical exaggeration. (Right) Synthetic record section generated from scenario illustrated to the left.

few free parameters of this fault model are burial depth, maximum depth, width, and percent change in velocity. For a background velocity model, we use a combination of the aforementioned shear wave velocity model from Yang, Atterholt, et al. (2022) for the shallowest 150 m and a local 1D velocity profile taken from the SCEC Unified Community Velocity Model (Small et al., 2017) for depths deeper than 150 m; we combine these two models using a linear interpolation. We then create a model fault zone by multiplying a section of the background model with an assigned rectangular geometry by a constant of proportionality.

We then use this model to perform synthetic tests that we can compare to our observations to assess the feasibility of this scatterer model. We generate these synthetics using Salvus (Afanasiev et al., 2019), a full waveform modeling software that simulates wave propagation using the spectral element method. We approximate the DAS array at Ridgecrest as a linear, 8 km array of strainmeters at the surface of our Earth model. We emplace a 2D double couple source with a 0.1 s half-duration Gaussian rate source time function 30 km east of the array at 10 km depth, a representative distance and depth for the earthquakes used in this study. We generate an adaptive mesh with which we can compute these synthetics up to 10.5 Hz with at least one element per wavelength. We use the same setup to perform tests of the fault geometry that we describe subsequently. We show an example of a simulation for a model with two faults with different geometries and velocity reductions in Figure 4. The faults in Figure 4 were parameterized using models for the faults associated with scatterers α and β that are proposed in the subsequent section. In particular, the fault on the left is parameterized as a 30% velocity reduction with a width of 20 m and a depth extent of 10–60 m. The fault on the right is parameterized as a 10% velocity reduction with a width of 50 m and a depth extent of 0–50 m. Both fault parameterizations are vertical. The resultant scattered waves in the synthetic wavefield match many of the first-order characteristics of the scattered waves in the observations of Figure 1. In particular, we have reproduced the observation of low-velocity scattered surface waves emanating from a narrow source. We can evaluate the similarities in the velocity content of the synthetic data and the observed data by computing the velocity spectrum of the scatterer component of the synthetic wavefield, as outlined in the preceding section. We show the velocity spectrum in Figure S3 in Supporting Information S1. The dispersion of the scattered wavefield in the synthetic test is a close match to the dispersion for the real data in Figure S2 in Supporting Information S1. Further, we see that secondary arrivals in the synthetics also produce scattered, dispersive waves. Secondary arrivals may thus explain why the scattered waves appear to reverberate in time. These simulations further confirm that these scatterers may be related to faults. As is clear in Figure 4, variations in the properties of the model fault zones create visually apparent differences in the strength of the scattered wavefield.

5. Constraining Fault Geometry

Now that we have a method of quantifying the degree of scattering in data and a means of simulating our observations using a reasonable model, we can constrain the properties of the sources of scattered waves by comparing features between the data and synthetics under this backprojection framework. As is evident in Figure 3, the peaks in these backprojection profiles have variant properties in space and frequency, and this variability may inform a better understanding of the faults that generate these peaks. Moreover, since we performed this backprojection for many events, we have an ensemble of profiles with which we can evaluate how well constrained the fault-zone properties that control these peak shapes are.

To generate our synthetics, we use the velocity model and source described in the preceding section. We also incorporate attenuation into our model. Since we do not have a priori estimates of the attenuation at this site, we parameterize the attenuation using the functional decay of the peaks from our backprojection profiles to obtain a rough estimate of the local attenuation structure. We assume an empirical relationship between shear wave velocity and attenuation structure, a common assumption when building an Earth model with heterogeneous attenuation structure (Graves & Pitarka, 2010), and may be denoted as $Q_\mu = cV_s$. To test the attenuation of surface waves away from a local scatterer, we define a fault zone according to the aforementioned simplified fault model with a width of 20 m, a depth extent of 0–100 m, and a 30% velocity reduction. We test several values for c and compare the spatial decay of the resultant synthetic peaks to those of peaks α and β at 4 Hz. We find that the data are best fit by a value of $c = 50$, a reasonable value for this relationship (Lai et al., 2020; Lin & Jordan, 2018). These peak comparisons are shown in Figure S4 in Supporting Information S1. This empirical relationship between attenuation and velocity is imperfect, as other parameters such as temperature and fluid content also control attenuation (Brocher, 2008; Eberhart-Phillips et al., 2014), and other factors such as structural heterogeneity can control surface wave amplitude (Bowden & Tsai, 2017). But, since we are only trying to obtain a reasonable attenuation parameterization for our forward model, this approximation is sufficient for our purposes.

To constrain the local fault zone properties, we note that the backprojection profiles shown in Figure 3 are functions of the frequency band in which we filter the data, and that each peak behaves differently with frequency. We investigate this property by evaluating the backprojection profiles for all narrow frequency bands for which we computed profiles in this study, with center frequencies ranging from 2 to 10 Hz. By plotting the mean profiles at each center frequency together, we can better inform our understanding of the behavior of the frequency dependence of individual scattering features along the array. We plot these mean profiles against center frequency and distance as a pseudocolor plot in Figure 5. As is evident in Figure 5, there are peaks that are traceable across a range of center frequencies, and there is a high degree of variability in the behavior of these peaks with frequency.

We then focus on the two most prominent peaks in this image, peak α and peak β, both of which are spatially correlated with USGS-mapped faults (USGS and CGS, 2022). By taking cross sections of the center frequency versus distance along array plot, we can determine the frequency dependence of these specific scatterers along this profile. Clearly, these peaks have different frequency dependences, which likely reflects a variability in the depth and geometry of the scattering fault zone. To discern the properties of these faults, we test different fault zone geometries to match these frequency dependent trends. Because the amplitudes of DAS data are not well understood, we only attempt to match the shape of the synthetic profile with the shapes of the peak profiles, and we thus normalize the synthetic profile amplitude by the ratio of the integrated amplitude of the mean peak profile to the integrated amplitude of the synthetic peak profile. We attempted to reproduce these frequency-amplitude trends by performing synthetic simulations that included fault zones with varying free parameters. These simulations were too expensive to perform a full grid search over all the fault model parameters, but by identifying patterns between fault zone parameterizations and subsequent simulated frequency-amplitude profiles, we were able to find fault zone models that produced good fits to the profile ensembles for both faults, as shown in Figure 5b. Indeed, reproducing the frequency-amplitude curves for the different peaks requires the use of variant fault zone parameterizations. Peak α is best fit by a 30% velocity reduction that is 20 m wide and spans 10–60 m depths. Peak β is best fit by a 10% velocity reduction that is 50 m wide and spans 0–50 m depths. The results for peak α suggest that we may be able to detect and constrain properties of small-scale buried faults.
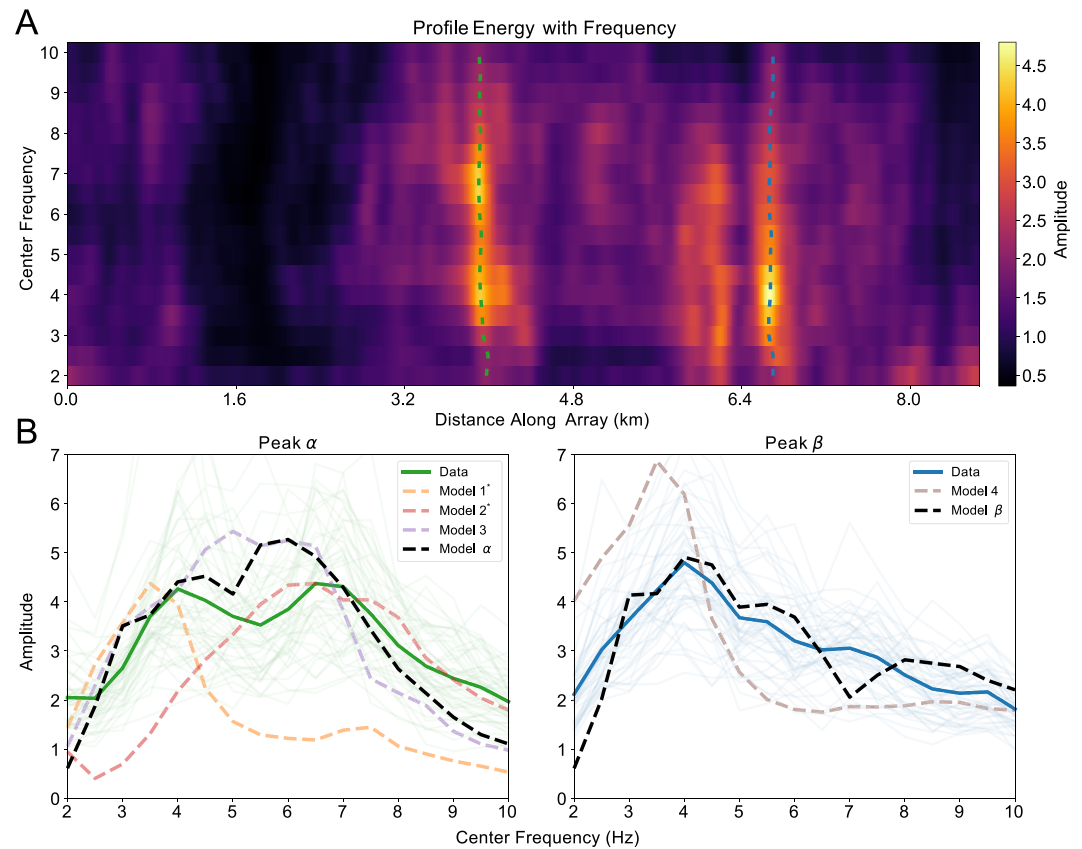
Figure 5. (a) Pseudocolor plot of mean backprojection amplitude plotted against center frequency and distance along array. Dotted green and dotted blue lines correspond to cross sections of this plot, associated with peaks α and β, respectively. (b) Plots of backprojection amplitude versus center frequency for the cross-sections shown in (a). Light green and light blue lines are the frequency-amplitude curves determined for a single event for peaks α and β, respectively. Dark green and dark blue lines are the mean frequency amplitude curves for peaks α and β, respectively. Dotted black lines correspond to the frequency-amplitude curves for our preferred fault zone model for each peak. Dotted colored lines are frequency amplitude curves for fault zone models with variant parameters to illustrate the constraints of this methodology. The parameters used for each model are given in Table S1 in Supporting Information S1. The asterisk in the legend indicates that, for visualization purposes, the corresponding model is normalized by the maximum height of the data curve rather than the integrated sum.

6. Discussion

The spatial correlation between the locations of sources of scattering and the mapped faults near the Ridgecrest DAS array shown in Figure 3 suggests that the source of at least some of these scatterers are faults, and thus DAS arrays can detect measurable signatures of fault zones. An example of the potential utility of this technique is readily available in this data set. In particular, peak α is located near, but is offset from, a mapped fault extending across the array. The Quaternary Fault Catalog (USGS and CGS, 2022) records this fault's location as inferred rather than directly observed; thus, we can use our backprojection profile to refine the location of this fault, treating peak α as a potential node of the fault trace. This node provides a stronger constraint on this fault's location near the town of Ridgecrest, CA, which has important implications for the location of possible static strain in the event of the activation of the Little Lake Fault Zone. This technique is generalizable to all DAS arrays that record seismicity, and may then be used elsewhere to systematically refine inferred fault locations and suggest the presence and locations of previously unmapped faults.

The profiles in Figure 3 bear a resemblance to results from distinct fault zone characterization methodologies, namely *S*-wave amplification analysis (e.g., Qiu et al., 2021). Both techniques can be used to locate faults at small spatial scales using the peak locations, but these techniques otherwise provide complimentary information. For example, the shape of the peaks in *S*-wave amplification profiles can be interpreted as an estimate of the lateral characteristics of the fault damage zone, while the shape of the peaks in this study are largely reflective of the

processing workflow and amplitude attenuation. But, the methodology presented in this study is more sensitive to small variations in the frequency of scattered waves that are reflective of characteristic dimensions of the fault zone, which includes constraints on the depth-dependence of the fault zone. Additionally, the methodology presented in this study is more readily applicable to DAS, both because DAS amplitudes are not well understood due to variability in coupling of the fiber and because DAS is particularly sensitive to low velocity surface waves.

The synthetic simulations in this study provide additional evidence that these chevron-like observations in DAS data are well-explained by fault zones. In particular, as shown in Figure 4, an approximation of a fault zone as a rectangular perturbation in velocity reproduces the first order features of these chevron-like observations. Additionally, the complexity in the frequency-amplitude curves shown in Figure 5 evidences a necessary variability in the finite properties of the scattering fault zones (Almuhaidib & Toksöz, 2014). But, importantly, this representation is non-unique, and the diversity of geologic heterogeneity in the upper crust suggests that features other than fault zones are likely responsible for at least some of the chevron-like observations we see in DAS data. Additionally, it is important to be careful when interpreting a backprojection image. Backprojection images are subject to spatial smearing due to constructive interference away from the true source location. Spatial smearing may bias frequency-amplitude curves by convolving contributions from multiple peaks. We minimize this form of biasing in this study by fitting only the most prominent peaks, which are spatially isolated from each other.

The geometric constraints we place on the faults in this study illustrate that, using DAS recorded earthquakes, we can constrain some aspects of the subsurface geometry of fault zones on the scale of tens of meters, potentially even for buried faults as is the case for peak α. Although these solutions are non-unique, they provide robust constraints on the approximate scaling of these subsurface structures. As stated prior, we were able to approach fault models that fit these data by identifying patterns in the relationship between fault zone geometry and the resultant synthetics. One interesting relationship, made clear in Figure 5, is related to the observation that peak β has a unimodal frequency-amplitude curve while peak α has a bimodal frequency-amplitude curve. The simulations suggest that two characteristic lengths produce distinct modes in these frequency-amplitude curves: the fault zone width and the fault zone depth extent. In particular, we obtain a unimodal frequency-amplitude curve when these lengths are the same (as with peak β) and a bimodal frequency-amplitude curve when these lengths are distinct (as with peak α), with the smaller characteristic dimension responsible for the highest frequency mode and vice versa. We demonstrate that variant characteristic dimensions can account for each frequency mode of peak α by running separate simulations for square-shaped buried faults, with velocity perturbations equivalent to the best fitting model for peak α, that extend up to 10 m depth with side lengths of 50 and 20 m, lengths which match the depth extent and width, respectively of the best fitting model for peak α. The amplitude-frequency curves of these simulations are plotted as Models 1 and 2 in Figure 5, respectively. Both of these models well approximate one of the individual modes of the bimodal data curve for peak α. Finally, although we normalize by amplitude, the magnitude of the velocity perturbation subtly changes the shape of the synthetic curves in our simulations in Figure 5; however, this is a weakly constrained parameter in this methodology.

Although this is not the first study to attempt to map fault zones using scattered waves in DAS data, a key contribution of this study is that it provides a framework to systematically locate the origins and discern the dimensions of these scatterers using the earthquake wavefield. Importantly, when using the earthquake wavefield, we are mostly looking at body-to-surface scattered waves, which have a different depth sensitivity than surface-to-surface scattered waves. In particular, body-to-surface wave scattering has a deeper depth sensitivity than surface-to-surface wave scattering because body waves can propagate at depth while surface waves have a frequency-limited depth extent (Barajas et al., 2022). But, body-to-surface wave scattering at a given frequency is still only sensitive to depths at which a scattering source can excite surface waves. Differences in sensitivity are important to consider when comparing this methodology to other scatterer characterization methods that use surface-to-surface wave scattering. Since we can only feasibly apply this technique between 2 and 10 Hz, this depth sensitivity constraint suggests that this methodology is only sensitive to the top few hundred meters. But, we suggest that the depth extents determined in this study are well-constrained by the data. To illustrate this, we perform a simulation for a fault with the same parameters as the best fitting model for peak β, but change the depth extent from 0–50 to 0–100 m. The frequency-amplitude curve for this simulation is plotted as Model 4 in Figure 5. This curve shows that for a deeper fault, we would expect to observe a frequency-amplitude curve more depleted in higher frequencies and enriched in lower frequencies. Recent techniques (e.g., Touma et al., 2022) have shown promise in imaging even deeper scatterers at high resolution using targeted array deployments. For imaging major fault

zones with deep structures, method integrated approaches may be useful for illuminating fault zone structures at all depths.

In Yang, Zhan, et al. (2022), the authors discern properties of the fault zone associated with peak α in this study as a 30% velocity reduction that is 35 m wide and spans 0–90 m depths. While this geometry is very close to our result and provides a useful verification of our technique, the differences that arise are likely due to the different sensitivities of the measurements and the different frequencies used to fit the fault model. Namely, the geometry of the faults discerned in this study were partially constrained by measurements over 6 Hz, which were not used to constrain the geometry in Yang, Zhan, et al. (2022). The higher frequency content used in this study likely explains why the characteristic dimensions discerned in this study are both smaller than those found in Yang, Zhan, et al. (2022). The higher frequency content may account for our ability to resolve a shallow burial depth. This fault burial depth is largely constrained by subtle variations in the peak shape. To illustrate this, we generate synthetics for a fault model with the same parameters as the best fitting model for peak α, but use a depth extent of 0–50 m instead of 10–60 m. The frequency-amplitude curve for this synthetic test is plotted as Model 3 in Figure 5. This result shows, that for an unburied fault, we achieve a slightly different shape that does not capture any separation of the high and low frequency modes of the data curve for peak α.

Finally we note that, although this study focused on relatively minor faults, this methodology can be readily extended to major fault zones, and requires only an across-fault DAS array and earthquake observations. Indeed, since the interrogation length for DAS units is increasing, and since many in situ fibers cross major faults, we can expect the number of DAS arrays sensing structure over major fault zones to increase rapidly over time. The technique presented in this paper presents an opportunity to leverage these DAS arrays to measure the fracture density and characteristics within major fault zones. Moreover, this study only covers one method with which DAS can be used to characterize major fault zones. Many of the aforementioned techniques which have previously used densely deployed conventional seismometers can be performed with DAS. The key challenges in applying these techniques, however, are that DAS provides a different observation than traditional seismometers, single component strain, and that DAS amplitudes are not well understood due to variability in coupling. These differences make some traditional fault characterization techniques, such as detecting fault zone head waves using particle motion analysis or measuring S-wave amplification, more difficult to apply using only DAS data. But, including some conventional inertial seismometers along a DAS array has the potential to diminish some of the challenges of DAS data (e.g., Lindsey et al., 2020; Muir & Zhan, 2021; Wang et al., 2018; Yang, Atterholt, et al., 2022). For the fault zone characterization case, including collocated three-component seismic sensors allows for amplitude calibration of DAS data and provides local particle motion observations. In this way, we can leverage the high station density and extensive deployments of DAS data while minimizing its limitations.

7. Conclusions

In this study we present a framework for the systematic location and characterization of fault zones using the DAS measured earthquake wavefield. This framework, which relies on the simple backprojection of the scattered wavefield following an earthquake, yields profiles of the scattered wave energy across the array. We apply this framework to 50 earthquake record sections recorded by a DAS array in Ridgecrest, CA, yielding an ensemble of profiles of scattered wave energy across the array. With these profiles, we identify numerous scattering peaks that are spatially well-correlated with mapped faults in the area, suggesting that these observed scattered waves are faults. Using these backprojection profiles, we suggest a correction to the location of one of the mapped faults in the area. Moreover, we present a model for these scattering sources as rectangular perturbations in the velocity structure, which is a simple approximation of a fault zone, and through simulations we show that this model reproduces first order observations of the observed scattered waves. Using this backprojection technique and these simulations, we establish a framework for using the locally scattered wavefield to evaluate shallow attenuation structure and infer characteristic dimensions of fault zones. We then apply this framework to the profiles computed for the Ridgecrest DAS array and consequently make claims about the fault zone structure near the array. We use the frequency decay of the profile peaks and synthetic simulations to image local faults at the scale of tens of meters, and with these images we distinguish between a fault that is surface-breaching and a fault that is buried.

Data Availability Statement

The data used in this study are available online at https://doi.org/10.22002/D1.20038 (Atterholt, 2022) as 30-s record sections that include the initial onset of the earthquake wavefield for the 50 high signal-to-noise ratio aftershocks recorded by the distributed acoustic sensing (DAS) array in Ridgecrest, CA referenced in this study. The simulations performed for this study were done using the software Salvus (Afanasiev et al., 2019), available at https://mondaic.com/. Figure 1 was made using The Generic Mapping Tools (GMT), version 6 (Wessel et al., 2019), available at https://www.generic-mapping-tools.org/.

References

Afanasiev, M., Boehm, C., van Driel, M., Krischer, L., Rietmann, M., May, D. A., et al. (2019). Modular and flexible spectral-element waveform modelling in two and three dimensions. *Geophysical Journal International*, *216*(3), 1675–1692. https://doi.org/10.1093/gji/ggy469

Ajo-Franklin, J., Tribaldos, V. R., Nayak, A., Cheng, F., Mellors, R., Chi, B., et al. (2022). The imperial valley dark fiber project: Toward seismic studies using DAS and telecom infrastructure for geothermal applications. *Seismological Society of America*, *93*(5), 2906–2919. https://doi.org/10.1785/0220220072

Allam, A. A., Ben-Zion, Y., & Peng, Z. (2014). Seismic imaging of a bimaterial interface along the Hayward fault, CA, with fault zone head waves and direct P arrivals. *Pure and Applied Geophysics*, *171*(11), 2993–3011. https://doi.org/10.1007/s00024-014-0784-0

Almuhaidib, A. M., & Toksöz, M. N. (2014). Numerical modeling of elastic-wave scattering by near-surface heterogeneities. *Geophysics*, *79*(4), T199–T217. https://doi.org/10.1190/geo2013-0208.1

Amos, C. B., Brownlee, S. J., Rood, D. H., Fisher, G. B., Burgmann, R., Renne, P. R., & Jayko, A. S. (2013). Chronology of tectonic, geomorphic, and volcanic interactions and the tempo of fault slip near Little Lake, California. *The Geological Society of America Bulletin*, *125*(7–8), 1187–1202. https://doi.org/10.1130/B30803.1

Ampuero, J., Vilotte, J., & Sánchez-Sesma, F. J. (2002). Nucleation of rupture under slip dependent friction law: Simple models of fault zone. *Journal of Geophysical Research*, *107*(B12), ESE2-1–ESE2-19. https://doi.org/10.1029/2001JB000452

Atterholt, J. (2022). Distributed acoustic sensing recorded Ridgecrest Earthquake aftershocks (1.0) [Dataset]. CaltechDATA. https://doi.org/10.22002/D1.20038

Atterholt, J., Zhan, Z., Shen, Z., & Li, Z. (2021). A unified wavefield-partitioning approach for distributed acoustic sensing. *Geophysical Journal International*, *228*(2), 1410–1418. https://doi.org/10.1093/gji/ggab407

Barajas, A., Margerin, L., & Campillo, M. (2022). Coupled body and surface wave sensitivity kernels for coda-wave interferometry in a three-dimensional scalar scattering medium. *Geophysical Journal International*, *230*(2), 1013–1029. https://doi.org/10.1093/gji/ggac091

Benioff, H. (1935). A linear strain seismograph. *Bulletin of the Seismological Society of America*, *25*(4), 283–309. https://doi.org/10.1785/BSSA0250040283

Bense, V., Gleeson, T., Loveless, S., Bour, O., & Scibek, J. (2013). Fault zone hydrogeology. *Earth-Science Reviews*, *127*, 171–192. https://doi.org/10.1016/j.earscirev.2013.09.008

Ben-Zion, Y., Peng, Z., Okaya, D., Seeber, L., Armbruster, J. G., Ozer, N., et al. (2003). A shallow fault-zone structure illuminated by trapped waves in the Karadere-Duzce branch of the North Anatolian Fault, western Turkey. *Geophysical Journal International*, *152*(3), 699–717. https://doi.org/10.1046/j.1365-246X.2003.01870.x

Bowden, D. C., & Tsai, V. C. (2017). Earthquake ground motion amplification for surface waves: Ground motions for surface waves. *Geophysical Research Letters*, *44*(1), 121–127. https://doi.org/10.1002/2016GL071885

Brocher, T. M. (2008). Key elements of regional seismic velocity models for long period ground motion simulations. *Journal of Seismology*, *12*(2), 217–221. https://doi.org/10.1007/s10950-007-9061-3

Catchings, R. D., Goldman, M. R., Li, Y., & Chan, J. H. (2016). Continuity of the West Napa–Franklin fault zone inferred from guided waves generated by earthquakes following the 24 august 2014 M$_w$ 6.0 South Napa earthquake. *Bulletin of the Seismological Society of America*, *106*(6), 2721–2746. https://doi.org/10.1785/0120160154

Cheng, F., Chi, B., Lindsey, N. J., Dawe, T. C., & Ajo-Franklin, J. B. (2021). Utilizing distributed acoustic sensing and ocean bottom fiber optic cables for submarine structural characterization. *Scientific Reports*, *11*(1), 5613. https://doi.org/10.1038/s41598-021-84845-y

Cochran, E. S., Li, Y.-G., Shearer, P. M., Barbot, S., Fialko, Y., & Vidale, J. E. (2009). Seismic and geodetic evidence for extensive, long-lived fault damage zones. *Geology*, *37*(4), 315–318. https://doi.org/10.1130/G25306A.1

Eberhart-Phillips, D., Thurber, C., & Fletcher, J. B. (2014). Imaging P and S attenuation in the Sacramento-San Joaquin Delta region, Northern California. *Bulletin of the Seismological Society of America*, *104*(5), 2322–2336. https://doi.org/10.1785/0120130336

Ellsworth, W. L. (2013). Injection-induced earthquakes. *Science*, *341*(6142), 1225942. https://doi.org/10.1126/science.1225942

Faulkner, D., Jackson, C., Lunn, R., Schlische, R., Shipton, Z., Wibberley, C., & Withjack, M. (2010). A review of recent developments concerning the structure, mechanics and fluid flow properties of fault zones. *Journal of Structural Geology*, *32*(11), 1557–1575. https://doi.org/10.1016/j.jsg.2010.06.009

Field, E. H., Arrowsmith, R. J., Biasi, G. P., Bird, P., Dawson, T. E., Felzer, K. R., et al. (2014). Uniform California earthquake rupture Forecast, version 3 (UCERF3)—The time-independent model. *Bulletin of the Seismological Society of America*, *104*(3), 1122–1180. https://doi.org/10.1785/0120130164

Fohrmann, M., Igel, H., Jahnke, G., & Ben-Zion, Y. (2004). Guided waves from sources outside faults: An indication for shallow fault zone structure? *Pure and Applied Geophysics*, *161*(11–12). https://doi.org/10.1007/s00024-004-2553-y

Freed, A. M., & Lin, J. (2001). Delayed triggering of the 1999 Hector Mine earthquake by viscoelastic stress transfer. *Nature*, *411*(6834), 180–183. https://doi.org/10.1038/35075548

Graves, R. W., & Pitarka, A. (2010). Broadband ground-motion simulation using a hybrid approach. *Bulletin of the Seismological Society of America*, *100*(5A), 2095–2123. https://doi.org/10.1785/0120100057

Harris, R. A., & Day, S. M. (1993). Dynamics of fault interaction: Parallel strike-slip faults. *Journal of Geophysical Research*, *98*(B3), 4461–4472. https://doi.org/10.1029/92JB02272

Harris, R. A., & Day, S. M. (1999). Dynamic 3D simulations of earthquakes on en echelon faults. *Geophysical Research Letters*, *26*(14), 2089–2092. https://doi.org/10.1029/1999GL900377

Jousset, P. (2019). Illuminating Earth's faults. *Science*, *366*(6469), 1076–1077. https://doi.org/10.1126/science.aaz7750

Joyce, K. E., Belliss, S. E., Samsonov, S. V., McNeill, S. J., & Glassey, P. J. (2009). A review of the status of satellite remote sensing and image processing techniques for mapping natural hazards and disasters. *Progress in Physical Geography: Earth and Environment*, *33*(2), 183–207. https://doi.org/10.1177/0309133309339563

Kiser, E., & Ishii, M. (2017). Back-projection imaging of earthquakes. *Annual Review of Earth and Planetary Sciences*, *45*(1), 271–299. https://doi.org/10.1146/annurev-earth-063016-015801

Kurzon, I., Vernon, F. L., Ben-Zion, Y., & Atkinson, G. (2014). Ground motion prediction equations in the San Jacinto fault zone: Significant effects of rupture directivity and fault zone amplification. *Pure and Applied Geophysics*, *171*(11), 3045–3081. https://doi.org/10.1007/s00024-014-0855-2

Lai, V. H., Graves, R. W., Yu, C., Zhan, Z., & Helmberger, D. V. (2020). Shallow basin structure and attenuation are key to predicting long Shaking duration in Los Angeles basin. *Journal of Geophysical Research: Solid Earth*, *125*(10), e2020JB019663. https://doi.org/10.1029/2020JB019663

Lay, V., Buske, S., Townend, J., Kellett, R., Savage, M., Schmitt, D. R., et al. (2021). 3D active source seismic imaging of the Alpine Fault zone and the Whataroa glacial valley in New Zealand. *Journal of Geophysical Research: Solid Earth*, *126*(12), 1–21. https://doi.org/10.1029/2021JB023013

Li, Z., Shen, Z., Yang, Y., Williams, E., Wang, X., & Zhan, Z. (2021). Rapid response to the 2019 Ridgecrest earthquake with distributed acoustic sensing. *AGU Advances*, *2*(2), e2021AV000395. https://doi.org/10.1029/2021AV000395

Liberty, L. M., St. Clair, J., & McKean, A. P. (2021). A broad, distributed active fault zone Lies beneath Salt lake City, Utah. *The Seismic Record*, *1*(1), 35–45. https://doi.org/10.1785/0320210009

Lin, Y.-P., & Jordan, T. H. (2018). Frequency-dependent attenuation of P and S waves in Southern California. *Journal of Geophysical Research: Solid Earth*, *123*(7), 5814–5830. https://doi.org/10.1029/2018JB015448

Lindsey, N. J., Dawe, T. C., & Ajo-Franklin, J. B. (2019). Illuminating seafloor faults and ocean dynamics with dark fiber distributed acoustic sensing. *Science*, *366*(6469), 1103–1107. https://doi.org/10.1126/science.aay5881

Lindsey, N. J., Rademacher, H., & Ajo-Franklin, J. B. (2020). On the broadband instrument response of fiber-optic DAS arrays. *Journal of Geophysical Research: Solid Earth*, *125*(2), e2019JB018145. https://doi.org/10.1029/2019JB018145

McGuire, J., & Ben-Zion, Y. (2005). High-resolution imaging of the Bear Valley section of the San Andreas Fault at seismogenic depths with fault-zone head waves and relocated seismicity. *Geophysical Journal International*, *163*(1), 152–164. https://doi.org/10.1111/j.1365-246X.2005.02703.x

Muir, J. B., & Zhan, Z. (2021). Seismic wavefield reconstruction using a pre-conditioned wavelet–curvelet compressive sensing approach. *Geophysical Journal International*, *227*(1), 303–315. https://doi.org/10.1093/gji/ggab222

Qin, L., Share, P.-E., Qiu, H., Allam, A. A., Vernon, F. L., & Ben-Zion, Y. (2020). Internal structure of the San Jacinto fault zone at the Ramona Reservation, north of Anza, California, from dense array seismic data. *Geophysical Journal International*, *224*(2), 1225–1241. https://doi.org/10.1093/gji/ggaa482

Qiu, H., Ben-Zion, Y., Catchings, R., Goldman, M. R., Allam, A. A., & Steidl, J. (2021). Seismic imaging of the M$_w$ 7.1 Ridgecrest earthquake rupture zone from data recorded by dense linear arrays. *Journal of Geophysical Research: Solid Earth*, *126*(7), e2021JB022043. https://doi.org/10.1029/2021JB022043

Ross, Z. E., Idini, B., Jia, Z., Stephenson, O. L., Zhong, M., Wang, X., et al. (2019). Hierarchical interlocked orthogonal faulting in the 2019 Ridgecrest earthquake sequence. *Science*, *366*(6463), 346–351. https://doi.org/10.1126/science.aaz0109

Scholtz, C. (2019). *The mechanics of earthquakes and faulting*. Cambridge University Press.

Share, P. E., & Ben-Zion, Y. (2018). A bimaterial interface along the northern San Jacinto fault through Cajon pass. *Geophysical Research Letters*, *45*(21), 11622. https://doi.org/10.1029/2018GL079834

Share, P. E., Qiu, H., Vernon, F. L., Allam, A. A., Fialko, Y., & Ben-Zion, Y. (2022). General seismic architecture of the Southern San Andreas fault zone around the Thousand Palms Oasis from a Large-N nodal array. *The Seismic Record*, *2*(1), 50–58. https://doi.org/10.1785/0320210040

Share, P.-E., Tábořík, P., Štěpančíková, P., Stemberk, J., Rockwell, T. K., Wade, A., et al. (2020). Characterizing the uppermost 100 m structure of the San Jacinto fault zone southeast of Anza, California, through joint analysis of geological, topographic, seismic and resistivity data. *Geophysical Journal International*, *222*(2), 781–794. https://doi.org/10.1093/gji/ggaa204

Small, P., Gill, D., Maechling, P. J., Taborda, R., Callaghan, S., Jordan, T. H., et al. (2017). The SCEC unified community velocity model software framework. *Seismological Research Letters*, *88*(6), 1539–1552. https://doi.org/10.1785/0220170082

Song, J., & Yang, H. (2022). Seismic site response inferred from records at a dense linear array across the Chenghai fault zone, Binchuan, Yunnan. *Journal of Geophysical Research: Solid Earth*, *127*(1), e2021JB022710. https://doi.org/10.1029/2021JB022710

Spica, Z. J., Castellanos, J. C., Viens, L., Nishida, K., Akuhara, T., Shinohara, M., & Yamada, T. (2022). Subsurface imaging with ocean-bottom distributed acoustic sensing and water phases reverberations. *Geophysical Research Letters*, *49*(2), e2021GL095287. https://doi.org/10.1029/2021GL095287

Spica, Z. J., Nishida, K., Akuhara, T., Pétrélis, F., Shinohara, M., & Yamada, T. (2020). Marine sediment characterized by ocean-bottom fiber-optic seismology. *Geophysical Research Letters*, *47*(16), e2020GL088360. https://doi.org/10.1029/2020GL088360

Thakur, P., Huang, Y., & Kaneko, Y. (2020). Effects of low-velocity fault damage zones on long-term earthquake behaviors on mature strike-slip faults. *Journal of Geophysical Research: Solid Earth*, *125*(8), e2020JB019587. https://doi.org/10.1029/2020JB019587

Touma, R., Aubry, A., Ben-Zion, Y., & Campillo, M. (2022). Distribution of seismic scatterers in the San Jacinto Fault Zone, southeast of Anza, California, based on passive matrix imaging. *Earth and Planetary Science Letters*, *578*, 117304. https://doi.org/10.1016/j.epsl.2021.117304

USGS & CGS. (2022). Quaternary fault and fold database for the United States. Retrieved from https://www.usgs.gov/natural-hazards/earthquake-hazards/faults

Wang, H. F., Zeng, X., Miller, D. E., Fratta, D., Feigl, K. L., Thurber, C. H., & Mellors, R. J. (2018). Ground motion response to an M$_L$ 4.3 earthquake using co-located distributed acoustic sensing and seismometer arrays. *Geophysical Journal International*, *213*(3), 2020–2036. https://doi.org/10.1093/gji/ggy102

Wang, Y., Allam, A., & Lin, F. (2019). Imaging the fault damage zone of the San Jacinto fault near Anza with ambient noise tomography using a dense nodal array. *Geophysical Research Letters*, *46*(22), 12938–12948. https://doi.org/10.1029/2019GL084835

Weng, H., Yang, H., Zhang, Z., & Chen, X. (2016). Earthquake rupture extents and coseismic slips promoted by damaged fault zones: Ruptures promoted by fault zones. *Journal of Geophysical Research: Solid Earth*, *121*(6), 4446–4457. https://doi.org/10.1002/2015JB012713

Wesnousky, S. G. (2008). Displacement and geometrical characteristics of earthquake surface ruptures: Issues and implications for seismic-hazard analysis and the process of earthquake rupture. *Bulletin of the Seismological Society of America*, *98*(4), 1609–1632. https://doi.org/10.1785/0120070111

Wessel, P., Luis, J. F., Uieda, L., Scharroo, R., Wobbe, F., Smith, W. H. F., & Tian, D. (2019). The generic mapping tools. Retrieved from https://www.generic-mapping-tools.org/

Xu, X., Sandwell, D. T., & Smith-Konter, B. (2020). Coseismic displacements and surface fractures from Sentinel-1 InSAR: 2019 Ridgecrest earthquakes. *Seismological Research Letters*, *91*(4), 1979–1985. https://doi.org/10.1785/0220190275

Yang, H., Duan, Y., Song, J., Jiang, X., Tian, X., Yang, W., et al. (2020). Fine structure of the Chenghai fault zone, Yunnan, China, constrained from teleseismic travel time and ambient noise tomography. *Journal of Geophysical Research: Solid Earth*, *125*(7), e2020JB019565. https://doi.org/10.1029/2020JB019565

Yang, Y., Atterholt, J. W., Shen, Z., Muir, J. B., Williams, E. F., & Zhan, Z. (2022). Sub-kilometer correlation between near-surface structure and ground motion measured with distributed acoustic sensing. *Geophysical Research Letters*, *49*(1), e2021GL096503. https://doi.org/10.1029/2021GL096503

Yang, Y., Zhan, Z., Shen, Z., & Atterholt, J. (2022). Fault zone imaging with distributed acoustic sensing: Surface-wave scattering.

Zigone, D., Ben-Zion, Y., Lehujeur, M., Campillo, M., Hillers, G., & Vernon, F. L. (2019). Imaging subsurface structures in the San Jacinto fault zone with high-frequency noise recorded by dense linear arrays. *Geophysical Journal International*, *217*(2), 879–893. https://doi.org/10.1093/gji/ggz069